Journal of Alloys and Compounds 757 (2018) 340–347

Contents lists available at ScienceDirect

Journal of Alloys and Compounds

journal homepage: http://www.elsevier.com/locate/jalcom

Secondary phases formation in lanthanum-doped titanium-zirconium-molybdenum alloy

Bo-liang Hu [a, b], Kuai-she Wang [a, b], Ping Hu [a, b, *], Yu-hang Zhou [a, b], Jie Deng [a, b], Wen-jing Chen [a, b], Peng-fa Feng [c], Ju-ping Zhang [c], Alex A. Volinsky [d], Hailiang Yu [a, e]

[a] School of Metallurgy Engineering, Xi'an University of Architecture and Technology, Xi'an 710055, China
[b] National and Local Joint Engineering Research Functional Center for Materials Processing, Xi' an University of Architecture and Technology, Xi'an 710055, China
[c] Jinduicheng Molybdenum Co., Ltd., Xi'an 710077, China
[d] Department of Mechanical Engineering, University of South Florida, Tampa FL 33620, USA
[e] School of Mechanical and Electrical Engineering, Central South University, Changsha 410083, China

ARTICLE INFO

Article history:
Received 2 December 2017
Received in revised form
7 May 2018
Accepted 8 May 2018
Available online 10 May 2018

Keywords:
Lanthanum-doped titanium-zirconium-molybdenum alloy
Secondary phase
Sintering
Thermodynamics calculations

ABSTRACT

Lanthanum-doped titanium-zirconium-molybdenum (La-TZM) alloys have good mechanical properties, including high strength and toughness due to complex secondary phases. Herein, the formation process of the secondary phases in the La-TZM alloy was revealed by thermodynamics calculations. The ΔG values of possible reactions during sintering were obtained. Results show that the formation process of the secondary phases was controlled by different reactions at different stages. At the first stage (0 −500 °C), the main reactions are listed as follows: $TiH_2+O_2(g)\rightarrow TiO_2+H_2\uparrow(g)$, $ZrH_2+O_2(g)\rightarrow ZrO_2+H_2\uparrow(g)$, $C_6H_{12}O_6\rightarrow[C]+ H_2O\uparrow$, $[C]+ O_2(g)\rightarrow CO_2(g)\uparrow$, $[C]+Mo\rightarrow MoC$, $La(NO_3)_3\cdot 6H_2O\rightarrow La_2O_3+NO_2\uparrow+ NO\uparrow+O_2\uparrow+H_2O$; $[C]+TiH_2\rightarrow TiC + H_2(g)\uparrow$, $[C]+ZrH_2\rightarrow ZrC + H_2(g)\uparrow$. At the secondary stage (680–960 °C), the dominant reactions include: $TiH_2\rightarrow Ti + H_2(g)\uparrow$, $ZrH_2\rightarrow Zr + H_2(g)\uparrow$. At the last stage (≥1200 °C), the primary reaction is $Ti + Zr+[O]\rightarrow ZrTiO_4$. The secondary phases in the La-TZM alloy include TiO_2, ZrO_2, ZrC, TiC, MoC, $ZrTiO_4$, La_2O_3 and the solid Ti and Zr phases. These results can guide the design of new ingredients for Mo alloys.

1. Introduction

Titanium-zirconium-molybdenum (TZM) alloys have high recrystallization temperature and high-temperature strength than pure molybdenum [1–3]. These alloys have been widely used in nuclear and aerospace industries as high-temperature dies, fusion-reactor diverter components and missile combustion chambers [4–7]. Oxide dispersion strengthened (ODS) molybdenum (or Mo-La) alloys consist of fine-grained molybdenum doped with lanthanum oxide particles and are suitable for nuclear applications with high enough strength at high temperature [8].

Solid solution strengthening and dispersion strengthening are effective methods to improve the mechanical properties of TZM alloys [9]. Small additives, such as oxides or carbides that act as grain refinement agents, are mixed into TZM alloys. Al_2O_3 additives can improve the oxidation and wear resistance of Mo [10–12]. Spinel ($MgAl_2O_4$), La_2O_3 and other rare earth oxide additives increase ductility of alloys [13,14]. Grain growth and structural failures can be inhibited by the formation of fine titanium and zirconium carbides at the grain boundaries in TZM alloys [13–15]. In addition to the aforementioned strengthening methods, we designed a new type of lanthanum-doped TZM (La-TZM) alloy using powder metallurgy. The oxidation resistance, mechanical properties, corrosion properties, ductile-to-brittle transition and recrystallization processes of the La-TZM alloy were studied [16–23]. Liu et al. [24] reported that the La_2O_3 secondary phase existed in $La(NO_3)_3$ doped Mo-La alloy. Liang et al. [25] investigated the formation mechanism of TiC, ZrC and Mo_2Zr in a TZM alloy during sintering. Fan et al. [26] found that Zr mostly formed Zr oxides and very little Zr diffused into the Mo matrix in a Mo-Zr alloy. Moreover, in the Mo-Ti alloy, some Ti diffused into Mo and formed Mo-Ti solid solution and the rest formed as $Mo_xTi_yO_z$ oxide particles.

* Corresponding author. School of Metallurgy Engineering, Xi'an University of Architecture and Technology, Xi'an 710055, China.
E-mail address: huping1985@126.com (P. Hu).

https://doi.org/10.1016/j.jallcom.2018.05.103
0925-8388/

Paul et al. [27] reported that the addition of nano-titanium carbide effectively improved the sintered density of TZM as well as hardness and flexural strength. TiC particles partially react with Mo in the TZM matrix during sintering according to the following reactions: $3Mo + TiC \rightarrow MoTi + Mo_2C$ and $MoO_x + TiC \rightarrow TiC_xO_y + Mo_2C$. Sujoy et al. [28] studied the phase stability in the Mo-Ti-Zr-C system using thermodynamic modeling. Mo_2Zr, Mo_2C, TiC, ZrC were made through spark plasma sintering (SPS) of carbide powders with ultrahigh purity. Li [29] prepared Mo-12Si-8.5 B alloys doped with lanthanum oxide by the liquid–liquid doping method. These alloys were composed of three phases, including α-Mo, Mo_3Si and $Mo_5SiB_2(T_2)$, as verified by TEM observations. However, they [27–29] did not investigate the formation process of secondary phases in high-temperature alloys by powder metallurgy, especially in TZM alloy.

Previous studies [30] show that doping lanthanum into traditional TZM alloys can significantly improve their strength (up to 1295 MPa) and toughness (up to 8%). The mechanical properties of La-TZM alloys are affected by different secondary particles that play different roles in these alloys. However, the formation process of the secondary phases in La-TZM alloys, including Ti, Zr, C and La additives has been rarely studied. In this study, we elucidate the formation process of secondary phases by using thermodynamics calculations. Moreover, the secondary particles of La-TZM alloy were investigated by X-ray diffraction (XRD), scanning electron microscopy (SEM) equipped with energy dispersive spectroscopy (EDS) and by transmission electron microscopy (TEM).

2. Experimental procedure

The nominal composition of the La-TZM alloy is listed in Table 1, which include TiH_2, ZrH_2, Mo powder, $C_6H_{12}O_6$, and $La(NO_3)_3 \cdot 6H_2O$ additives. The details are listed as follows: pure Mo powder (FMo-1, ≤6 μm, Jinduicheng Molybdenum Co., Ltd.), TiH_2 powder (≤5 μm, Xi'an Baode Powder Metallurgy Co., Ltd.), ZrH_2 powder (≤4 μm, Xi'an Baode Powder Metallurgy Co., Ltd.), organic carbon ($C_6H_{12}O_6$), and $La(NO_3)_3$ (Ganzhou Jiarun New Materials Co., Ltd.). The alloy was doped with lanthanum by the solid-liquid doping method.

The samples were fabricated through the following steps: mixing the powder, ball milling, compacting and sintering, followed by rolling into a 0.6 mm thick plate (90% deformation rate), as shown in Fig. 1. In addition, Fig. 1 also shows the content of impurity elements in FMo-1 powder. O impurities are less than 0.15 wt % and other elements are less than 0.015 wt %.

Fig. 2 shows the sintering process of the La-TZM alloy. The powders were heated from 25 °C to 1950 °C. According to the powder metallurgy of Mo alloy, the powders undergo a series of physical and chemical changes during the sintering process: evaporation of water or volatile organic material, removal of adsorbed gas, stress relief, reduction in surface oxide powder particles, interparticle mass transfer, recrystallization and grain growth [31]. Thus, the process was divided into five stages to make sure that each process is completed in a hydrogen furnace.

XRD (Bruker D8 Advance) was used to investigate the phases in the material formed during sintering. The microstructure of secondary phases was characterized by SEM equipped with EDS (JSM-6460LV) and TEM (JEM-200CX). TEM samples were prepared by grinding and polishing to 30 μm thickness foil, followed by twinjet electropolishing with a solution of alcohol and 5% $HClO_4$, N-butanol and methanol at −40 °C.

Table 1
Nominal composition of the La-TZM alloy (wt.%).

Sample	Ti	Zr	C	La	O	Fe	Ni	Mo
La-TZM	0.65	0.07	0.03	0.983	0.44	0.013	0.007	Balance

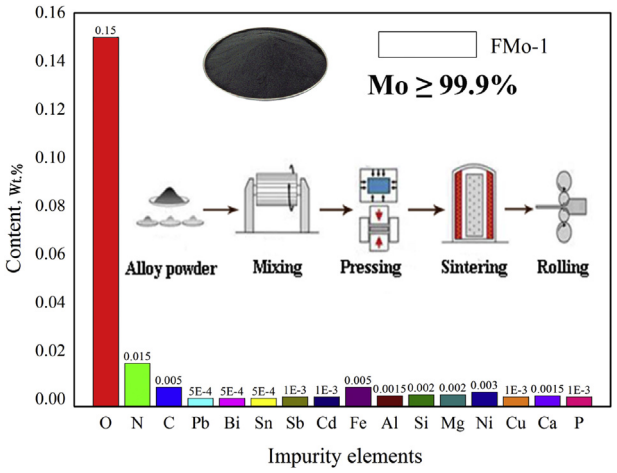

Fig. 1. Schematic illustration of fabrication processes of La-TZM alloy and content of impurity elements in FMo-1 powder.

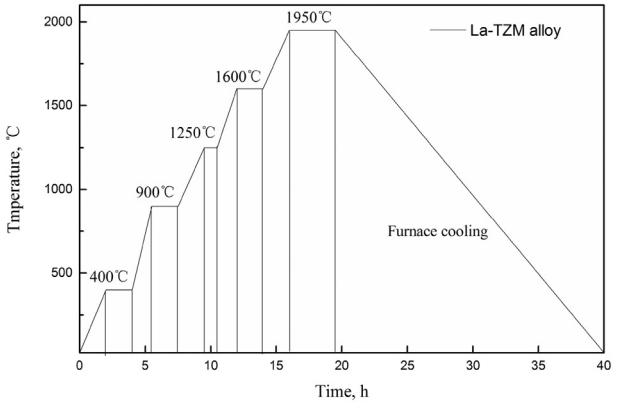

Fig. 2. Sintering process of the La-TZM alloy.

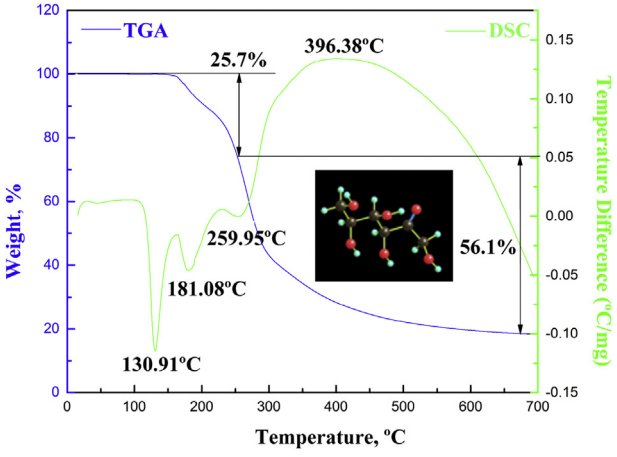

Fig. 3. TGA and DSC curves for fructose ($C_6H_{12}O_6$).

3. Results and discussion

3.1. Differential thermal analysis of fructose decomposition

The C element is added in powders by fructose ($C_6H_{12}O_6$). Fig. 3 shows the differential scanning calorimetry (DSC) and thermal gravimetric analyzer (TGA) curves of fructose at argon atmosphere. The DSC curve has three endothermic peaks below 300 °C and TGA curve shows weight loss. There is an endothermic peak at 364 °C and the TGA curve weight loss reaches 70.33% between 215 °C and 676 °C. The TGA curve is stable when the temperature reaches 676 °C. The total weight loss of TGA curve is 81%, including moisture, so the thermal decomposition of fructose mainly exists in the form of C atoms or activated atomic carbon at the molecular level at 100–676 °C.

3.2. Thermodynamics calculations of the secondary phases formation

The chemical thermodynamics is used to study the energy exchange process, which determines the direction and limitation of the reaction, whether $\Delta_r G_m^\theta(T)$ is less than zero, and the problem of chemical thermodynamics must be solved based on thermodynamics calculations [31]. Calculation formulas of $\Delta_r H_m^\theta(T)$, $\Delta_r S_m^\theta(T)$ and $\Delta_r G_m^\theta(T)$ are shown as follows:

$$\Delta_r H_m^\theta(T) = \sum V_B \Delta_f H_m^\theta(T) \tag{1}$$

$$\Delta S_m^\theta(T) = \sum V_B \Delta_f S_m^\theta(T) \tag{2}$$

$$\Delta_r G_m^\theta(T) = \sum V_B \Delta_f G_m^\theta(T) = \Delta_r H_m^\theta \Delta(T) - \Delta_r S_m^\theta \Delta(T) \tag{3}$$

Here, T is the temperature, $\Delta rH_m^\theta \Delta(T)$ and $\Delta rG_m^\theta \Delta(T)$ represent the standard enthalpy of formation and standard Gibbs free energy. These values are obtained from the thermodynamics general manual. For any temperature T, $\Delta_r H_m^\theta \Delta(T)$ and $\Delta_r G_m^\theta \Delta(T)$ can be calculated according to the design method through the state function:

$$\Delta_r H_m^\theta(T) = \Delta r H_m^\theta + \int_{298.15}^{T} \Delta C_P dT \tag{4}$$

$$\Delta_r S_m^\theta(T) = \Delta_r S_m^\theta + \int_{298.15}^{T} \Delta C_P d\ln T \tag{5}$$

If the molar heat capacity follows the $C_{p.m} = a + bT + cT^2$ form at constant pressure, then

$$\Delta C_p = \Delta a + \Delta bT + \Delta cT^2 \tag{6}$$

Plugging Eq. (6) into Eq. (4) and Eq. (5), and then integrating yields:

$$\Delta_r H_m^\theta(T) = \Delta H_0 + \Delta aT + \Delta bT^2/2 + \Delta cT^3/3 \tag{7}$$

$$\Delta_r S_m^\theta(T) = \Delta a + IR + \Delta a \ln T + \Delta bT + \Delta cT^2/2 \tag{8}$$

$$\Delta_r G_m^\theta(T) = \Delta H_0 - IRT + \Delta aT \ln T - \frac{\Delta bT^2}{2} - \Delta cT^3/6 \tag{9}$$

Here, ΔH_0 and I are integration constants. Solving for $T = 0$ °C yields:

$$\Delta H_0 = \Delta r H_m^\theta(298.15) - 298.15\Delta a - \frac{298.15^2}{2}\Delta b + \frac{298.15^3}{3}\Delta c \tag{10}$$

All $\Delta_r H_m^\theta$, $\Delta_r G_m^\theta$ and heat capacity data were manually checked. The above formula can be used to calculate the $\Delta_r H_m^\theta(T)$ and $\Delta_r G_m^\theta(T)$.

However, the computational complexity of this method is relatively high. Some reactions can be found from the corresponding $\Delta_r G_m^\theta(T)$ at various temperatures by using the thermodynamics manual. The standard Gibbs free energy expression is $\Delta_r G_m^\theta(T) = A + BT$.

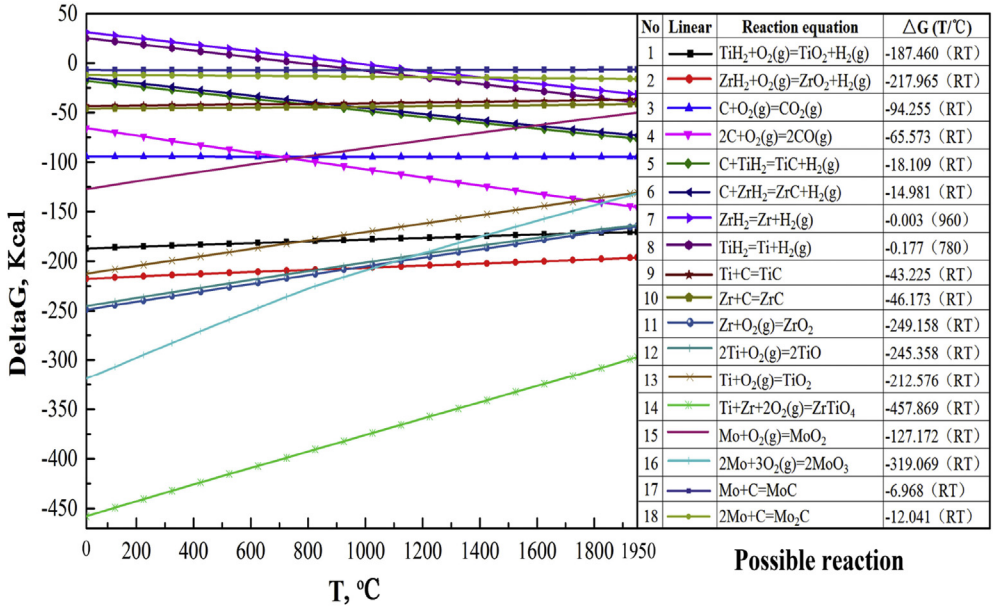

No	Linear	Reaction equation	ΔG (T/℃)
1		$TiH_2+O_2(g)=TiO_2+H_2(g)$	-187.460 (RT)
2		$ZrH_2+O_2(g)=ZrO_2+H_2(g)$	-217.965 (RT)
3		$C+O_2(g)=CO_2(g)$	-94.255 (RT)
4		$2C+O_2(g)=2CO(g)$	-65.573 (RT)
5		$C+TiH_2=TiC+H_2(g)$	-18.109 (RT)
6		$C+ZrH_2=ZrC+H_2(g)$	-14.981 (RT)
7		$ZrH_2=Zr+H_2(g)$	-0.003 (960)
8		$TiH_2=Ti+H_2(g)$	-0.177 (780)
9		Ti+C=TiC	-43.225 (RT)
10		Zr+C=ZrC	-46.173 (RT)
11		$Zr+O_2(g)=ZrO_2$	-249.158 (RT)
12		$2Ti+O_2(g)=2TiO$	-245.358 (RT)
13		$Ti+O_2(g)=TiO_2$	-212.576 (RT)
14		$Ti+Zr+2O_2(g)=ZrTiO_4$	-457.869 (RT)
15		$Mo+O_2(g)=MoO_2$	-127.172 (RT)
16		$2Mo+3O_2(g)=2MoO_3$	-319.069 (RT)
17		Mo+C=MoC	-6.968 (RT)
18		$2Mo+C=Mo_2C$	-12.041 (RT)

Fig. 4. Possible thermodynamic equilibrium reactions during sintering.

Possible reactions are shown in Fig. 4 (reactions 1–16), along with the corresponding free energy. First, the reactions cannot proceed when △G is positive according to thermodynamics. Thus, reactions 1–16 will not happen above the 960 °C due to their negative △G. O can react with Mo, forming MoO_3 because △G is the lowest. Then ZrH_2 reacts with O, producing H_2. Because △G for the reaction (2) is lower than that of (1), reaction (2) is more likely to happen, and then the reaction (1) happens. After that C reacts with O, producing CO_2. Because △G of the reaction (3) is lower than (4), reaction (3) is more likely to happen. Reaction (5) and (6) start when oxygen is depleted by C. The reactions (8) and (7) happen at 780 °C and 960 °C. Similarly, reaction (14) will happen when Ti and Zr form by reactions (7) and (8). △G for reaction (14) is lower than for (9-14). C reacts more easily with Ti and Zr. Reactions (9) and (10) are more likely to happen because △G for reactions (9) and (10) is lower than for (17) and (18). Reactions (17) and (18) may happen because △G is lower than zero. As a result, when the temperature reaches 1950 °C, reactions (11-13), (15) and (17) may happen as well at atmospheric pressure. Therefore, $ZrTiO_4$, ZrO_2, TiO, TiO_2, MoO_2 and MoO_3 phases may appear in the La-TZM alloy during sintering.

3.3. Thermogravimetric analysis

Possible reactions characterized by thermogravimetric mass spectrometry (TG-MS) are shown in Fig. 5. The test sample was made using the La-TZM alloys, which were mixed and dried at 25 °C in argon gas. The sample weight for the TG-MS test was 52.6 mg. The H_2O, NO, NO_2, CO_2 and H_2 gases were vented out during the heating process and the weight loss was 6.25 mg. Weight loss

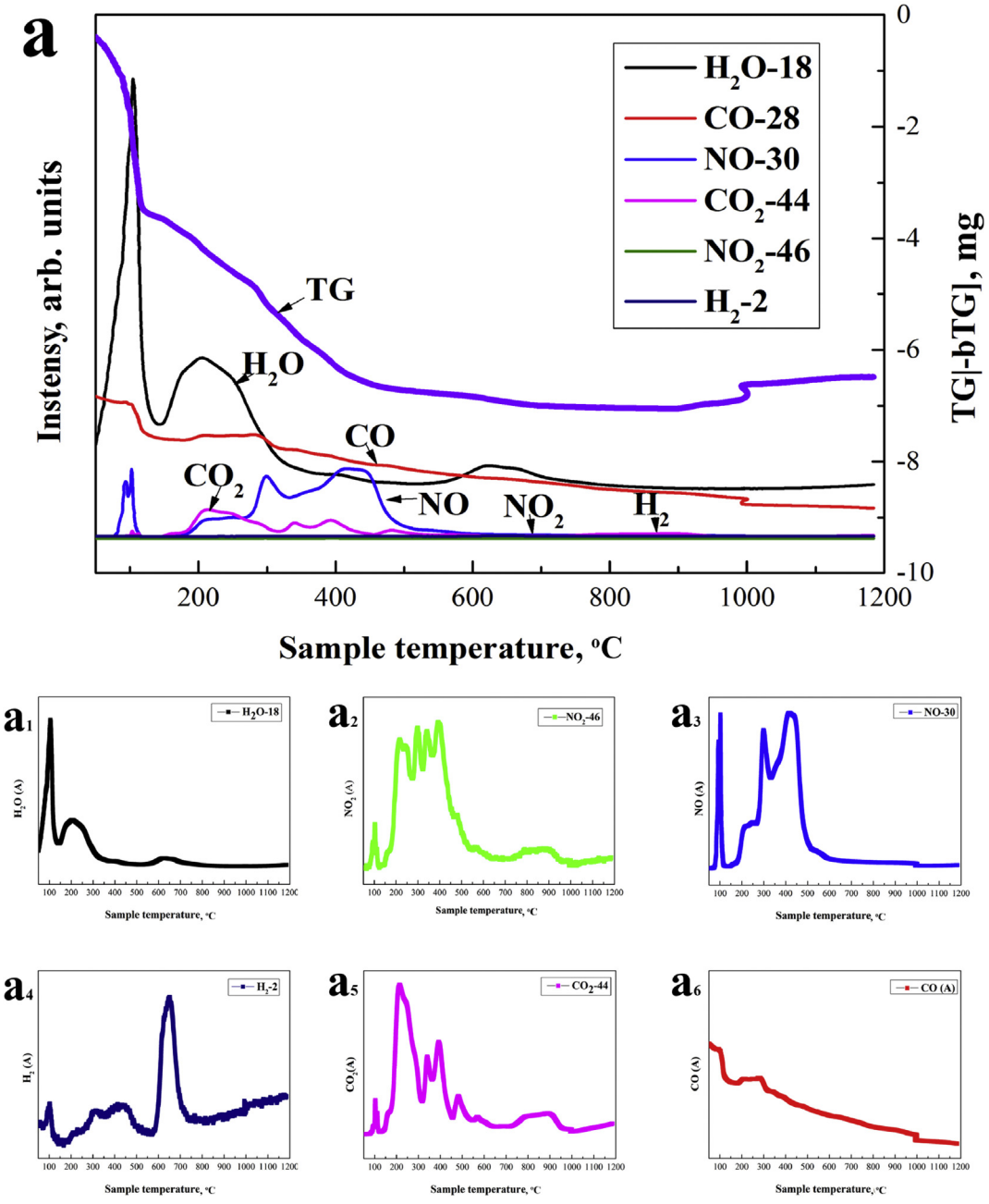

Fig. 5. TG-MS of La-TZM mixed powders (a, TG-MS curve; a_1, MS curve of H_2O; a_2, MS curve of NO_2; a_3, MS curve of NO; a_4, MS curve of H_2; a_5, MS curve of CO_2; a_6, MS curve of CO).

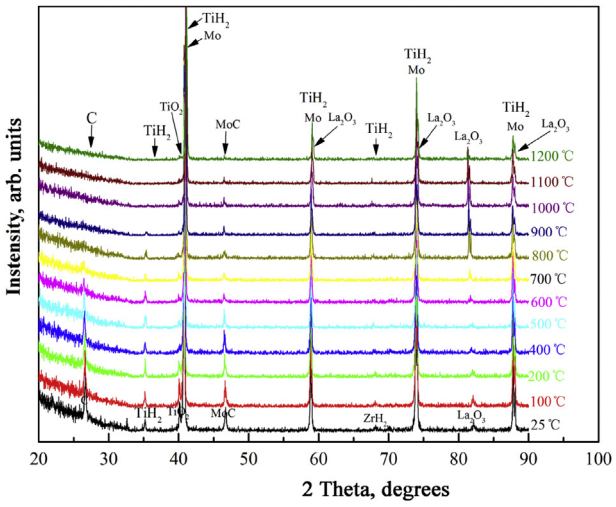

Fig. 6. XRD patterns of La-TZM from 25 °C to 1200 °C.

accounted for 12% of the total mass in Fig. 5a. Water vapor was mainly produced below 300 °C, as shown in Fig. 5a$_1$, and NO, NO_2 and CO_2 were generated below 500 °C, while hydrogen was mainly produced below 1000 °C, especially at 100 °C and 650 °C.

TG-MS revealed that a small amount of H_2 was generated at 100–500 °C because TiH_2 and ZrH_2 reacted with [O] and TiH_2 and ZrH_2 reacted with [C], which is decomposition by organic carbon. The reaction system releases CO_2 when the temperature is 100–1000 °C because [C] reacts with [O], as shown in Fig. 5a$_5$. NO and NO_2 are produced by La $(NO_3)_3$ decomposition reaction until 400 °C, as shown in Fig. 5a$_2$ and a$_3$. When the system temperature is up to 650 °C, the system releases lots of H_2 due to the decomposition of TiH_2. When the temperature continued to rise to 960 °C, the system let out a small amount of H_2 for ZrH_2 decomposition in Fig. 5a$_4$. The TG-MS curves reflect the reaction processes in the whole system.

The phases of powder sample at different temperatures are shown in Fig. 6. The phases are tested from 25 °C to 1200 °C. The test environment was vacuum ($\leq 10^{-2}$ MPa).

High-temperature XRD results show the molybdenum phase stability during the reaction process. At the start, the main phases are Mo, TiO_2, TiH_2, ZrH_2, C, MoC and La_2O_3. After that, the characteristic peak of C element rises from 25 °C to 400 °C, and then reduces from 400 °C to 700 °C. The TiH_2 and ZrH_2 characteristic peaks have been weakened at high temperature, until they disappeared at 1200 °C. The characteristic peaks of La_2O_3 are gradually strengthened. Liu [32] detected the La_2O_3 particles in the NS-Mo, which showed up in particles diffraction pattern. The last stable phases mainly include Mo, TiO_2, MoC and La_2O_3, but Mo characteristic peak shifts to the left. In fact, such secondary carbide-forming reactions are quite common in ferrous alloys. Alloys, such as TZM (Mo-0.5Ti-0.08Zr-0.03C) and TZC (Mo-1.2Ti-0.3Zr-0.1C), owe much of their high-temperature strength and microstructural stability to MC and M_2C carbide phases [33].

At the beginning, system has generated TiO_2, C, MoC and La_2O_3 because of the drying process after mixing powder. With the increase of test temperature, TiH_2 gradually disappears at 900 °C, ZrH_2 gradually disappears at 1100 °C, but La_2O_3 phase does not disappear. C element mainly produces organic carbon decomposition, but C element characteristic peak disappears after 600 °C. C reacts with O, TiH_2 and ZrH_2 and gets consumed. La_2O_3 characteristic peak is formed by $La(NO_3)_3 \cdot 6H_2O$ decomposition, and it does not react with other substances. The characteristic peaks of TiH_2 and ZrH_2 disappear because of the TiH_2 and ZrH_2 reactions with [O] and [C].

The secondary phases of TiC and ZrC are difficult to be detected by XRD because of their small amount. For the XRD, the phase cannot be measured accurately when its content is less than 1%, therefore, EDS and TEM diffraction were used to detect some products.

The morphology and distribution of secondary phases are shown in Fig. 7. The secondary phases are in huge quantity and are distributed uniformly. Majority of secondary phases have spherical shape and a small portion of secondary phases are in the form of irregularly shaped particles. In Fig. 7a, a, large amount of secondary phases are mainly on the grain boundaries and smaller secondary phases are mainly in the grain. There are different sizes of pores at grain boundaries.

EDS analyses reveal that the secondary phase included C, O, Ti, Zr, Mo and La elements in Fig. 7b. The major ingredients of the secondary phase are O, Ti and La. The secondary phase of ZrO_2 and TiO_2 was formed before the La_2O_3, so La_2O_3 was formed on the particles surface of ZrO_2 and TiO_2. The secondary phase size is larger than others because large TiH_2 and ZrH_2 powders are oxidized in situ. Some secondary phases were aggregated by La_2O_3 and TiO_2, based on atomic ratio calculations. The right secondary phase is formed by Mo and oxide elements. Li [29] showed images of La_2O_3 particles in Mo_5SiB_2 when doping lanthanum oxide into Mo–12Si–8.5 B alloys by the liquid–liquid doping method.

Fig. 8 shows some secondary phases in La-TZM alloys and their corresponding diffraction pattern. From the secondary phase morphology, different secondary phases appear in the La-TZM alloy. As seen from the diffraction pattern (Fig. 8a–d), the secondary phases include TiC, ZrC, $ZrTiO_4$ and MoC, but La_2O_3 particles are not detected in the alloy. The reason is that the La_2O_3 particles

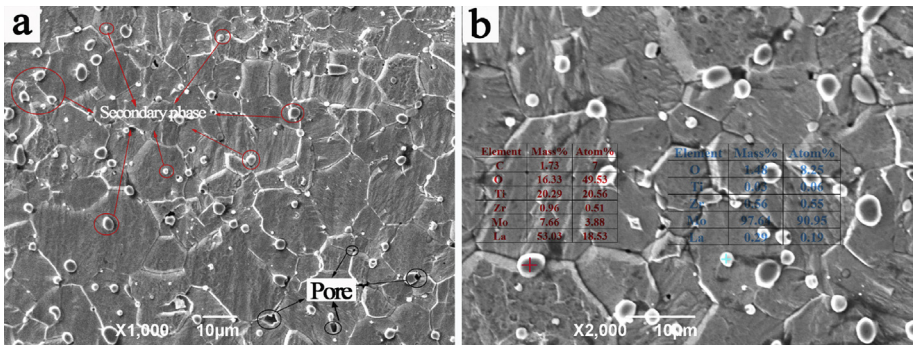

Fig. 7. SEM images and EDS spectra of secondary phases of the La-TZM alloy.

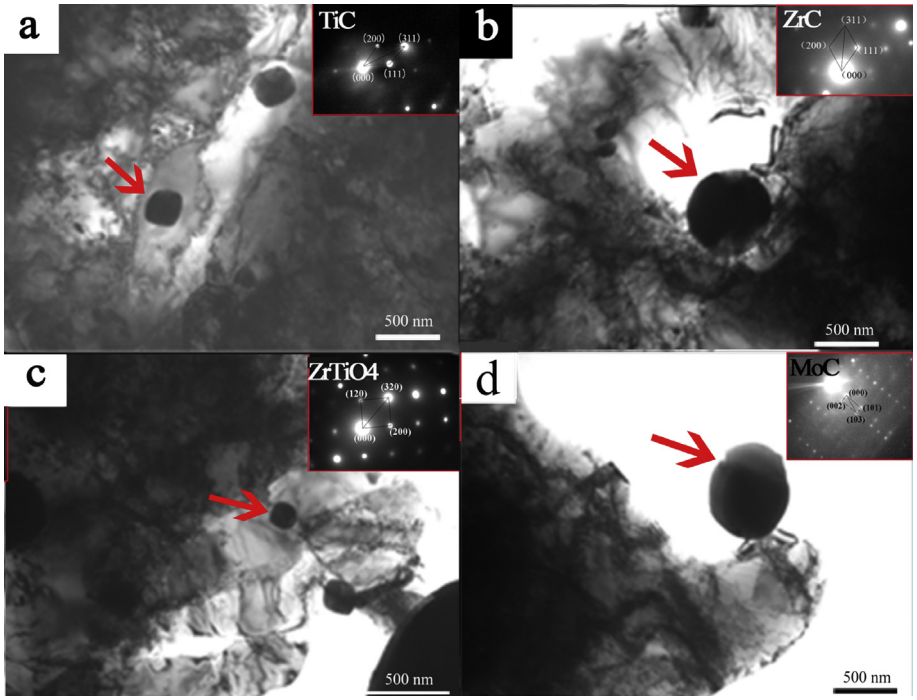

Fig. 8. TEM images of La-TZM microstructure (a, diffraction pattern of TiC; b, diffraction pattern of ZrC; c, diffraction pattern of $ZrTiO_4$; d, diffraction pattern of MoC).

are wrapped by other elements. This is seen in the EDS analysis in Fig. 7b. The particle size of TiC is about 200 nm, and $ZrTiO_4$ is 50 nm, however, the particle size of MoC and ZrC is about 500 nm. The morphology of secondary phase is similar to spheres. This plateau in the carbide fraction is contrary to Wadsworth's [34] thermodynamic calculations for MC carbide precipitates (specifically HfC) in tungsten and molybdenum alloys. According to the characteristics of powder metallurgy, after mixing powder, all kinds of reactions during sintering will be prioritized based on coacervate phase interface of particles. With the densification and solid-state diffusion of the elements, reactions occur between the aggregate particles, sub-grain boundaries or grain boundaries. Alloying elements can easy form carbides. Ti and Zr form carbides with C atoms precipitate out of molybdenum substrate during cooling [25]. However, $ZrTiO_4$ was also formed in the La-TZM alloy due to the O atoms precipitated out of molybdenum substrate. This enlarges secondary phases in the TZM alloy.

The content of O in the Mo lattice is about $(20–40) \times 10^{-6}$. O reacted with solid Zr and Ti at high temperature. The secondary $ZrTiO_4$ phase is formed, but it is of smaller size and weight in the alloy.

Secondary phases in La-TZM and product formed during sintering were analyzed based on thermodynamics calculations. Micro-characterization results of the secondary phases products by

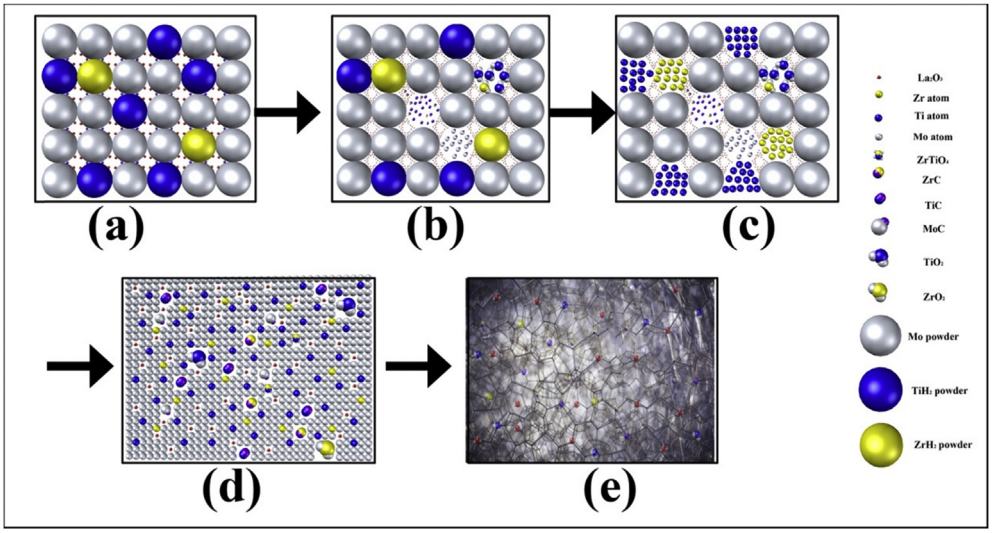

Fig. 9. Schematic diagram of secondary phases formation in the La-TZM alloy: (a) mixed powder; (b) organic carbon and $La(NO_3)_3$ decomposition, TiO_2, ZrO_2 and MoC form, part of TiC and ZrC form; (c) TiH_2 and ZrH_2 decomposition; (d) Ti and Zr solid and form $ZrTiO_4$; (e) secondary phases exist in the La-TZM alloy finally.

can be obtained from the following reactions below 1200 °C:

$$TiH_2+O_2(g) \rightarrow TiO_2+H_2(g) \quad (11)$$

$$ZrH_2+O_2(g) \rightarrow ZrO_2+H_2(g) \quad (12)$$

$$C_6H_{12}O_6 \rightarrow [C]+H_2O \quad (13)$$

$$[C]+O_2(g) \rightarrow CO_2(g)\uparrow \quad (14)$$

$$[C]+TiH_2 \rightarrow TiC + H_2(g)\uparrow \quad (15)$$

$$[C]+ZrH_2 \rightarrow ZrC + H_2(g)\uparrow \quad (16)$$

$$La(NO_3)_3\cdot 6H_2O \rightarrow La_2O_3+NO_2\uparrow+NO\uparrow+O_2\uparrow+H_2 \quad (17)$$

$$[C]+Mo \rightarrow MoC \quad (18)$$

$$TiH_2 \rightarrow Ti + H_2(g)\uparrow \quad (19)$$

$$ZrH_2 \rightarrow Zr + H_2(g)\uparrow \quad (20)$$

$$Ti + Zr+[O] \rightarrow ZrTiO_4 \quad (21)$$

Generated secondary phases mainly include a small amount of TiO_2, ZrO_2, TiC, ZrC, La_2O_3, MoC, $ZrTiO_4$ Ti and Zr, and then Ti and Zr solid solution in the matrix. The whole process is shown in Fig. 9. It is assumed that solid powder and additives are in the granular form.

3.4. Experimental results and thermodynamic assessment

Thermodynamic calculations provide the possibility of various reactions in the La-TZM alloy. Fig. 4 lists 18 kinds of possible reactions in the 25–1950 °C temperature range, along with the corresponding ΔG values. At the first stage, a small amount of hydrogen is released at 100 °C in Fig. 5a$_4$. Only TiH_2 and ZrH_2 are oxidized by oxygen or restored by carbon, however, fructose begins to decompose to carbon above 100 °C in Fig. 4. The reason is that the TiH_2 and ZrH_2 are oxidized by oxygen. After that, hydrogen gas is generated at 300–500 °C, as shown in Fig. 5a$_4$, which is only produced with TiH_2 and ZrH_2 restored by carbon. For this reason, TiO_2, ZrO_2, TiC and ZrC are formed in the Mo matrix. According the thermodynamic assessment, the ΔG values of the TiH_2 and ZrH_2 reactions with oxygen are less than with carbon. The TiH_2 and ZrH_2 are oxidized easier than reduced. This result is consistent with the high temperature XRD, SEM and TEM data in Figs. 6–8. At the same time, the CO_2 gas is exhausted from the system at 100–500 °C in Fig. 5a$_5$, for which the ΔG of CO_2 is less than CO in the 100–700 °C temperature range in Fig. 4. Thus, the system cannot release CO in Fig. 5a$_6$. C atoms also react with Mo after O on the powder surface runs out of C. The ΔG of the MoC reaction is less than zero at 100–500 °C. The result is revealed in Figs. 6 and 8.

From the MS curve, H_2 gas is produced at about 700 °C and 1000 °C. The ΔG of TiH_2 is less than zero when the temperature is higher than 780 °C, and ZrH_2 above 960 °C in Fig. 4. Thermodynamics calculation results are consistent with the experimental results. After Ti and Zr atoms are decomposed by TiH_2 and ZrH_2, $ZrTiO_4$ is most easily formed because ΔG is the smallest in all reactions. The $ZrTiO_4$ is detected in the alloy by TEM, as shown in Fig. 8.

Fig. 9 shows the formation process of secondary phases in the La-TZM alloy. All the powders are mixed uniformly by mixing and ball-milling at the first stage, but powders exist in different form in Fig. 9a. TiH_2 and ZrH_2 powders (≤5 μm) replace Mo (≤6 μm) when the granularity of TiH_2 and ZrH_2 powders reaches 83.3% of the Mo powder. However, other tiny powders exist in the Mo powder. The reaction of $C_6H_{12}O_6 \rightarrow [C]+H_2O$ and $La(NO_3)_3\cdot 6H_2O \rightarrow La_2O_3+NO_2\uparrow+NO\uparrow+O_2\uparrow +H_2O$ can proceed below 500 °C. The reaction of $TiH_2+O_2(g) = TiO_2+H_2(g)$, $ZrH_2+O_2(g) = ZrO_2+H_2(g)$, $[C]+O_2(g) \rightarrow CO_2(g)\uparrow$, $[C]+TiH_2 \rightarrow TiC + H_2(g)\uparrow$ $[C]+ZrH_2 \rightarrow ZrC + H_2(g)\uparrow$ and $[C]+Mo \rightarrow MoC$ can proceed between 25 °C and 500 °C in Fig. 9b. Then $TiH_2 \rightarrow Ti + H_2(g)$ begins to decompose. After that $ZrH_2 \rightarrow Zr + H_2(g)$ begins to decompose, as shown in Fig. 8c. Then Ti and Zr become solid in the lattice. The solid solution O exists in molybdenum lattice, so $Zr + Ti+2O_2(g) \rightarrow ZrTiO_4$ starts to react, as shown in Fig. 9d. TiO_2, ZrO_2, ZrC, TiC, La_2O_3, MoC and $ZrTiO_4$ exist in the La-TZM alloy, as shown in Fig. 9e. Most of the secondary phases exist at the grain boundaries and the others exist transgranular in Figs. 7a and 9e.

4. Conclusions

(1) Thermodynamic calculations can provide criteria for reactions of secondary phases. TG-MG and high temperature XRD verify the reactions.
(2) The whole reaction process includes the following below 1200 °C. At the first stage (0–675.96 °C) TiH_2 and ZrH_2 react with O_2 and then form TiO_2 and ZrO_2. Fructose gradual decomposition generates carbon at the molecular level, and then carbon reacts with oxygen, Mo, TiH_2 and ZrH_2 generate carbon dioxide, MoC, titanium carbide, zirconium carbide and hydrogen. At the same time, $La(NO_3)_3\cdot 6H_2O$ decomposes into lanthanum oxide, nitric oxide and nitrogen dioxide. At the secondary stage (680-960 °C) TiH_2 and ZrH_2 decomposition generates titanium, zirconium and hydrogen. At the last stage (≥1200 °C) titanium and zirconium generate $ZrTiO_4$ by reacting with solid solution oxygen.
(3) The secondary phases of La-TZM alloy include TiO_2, ZrO_2, ZrC, TiC, MoC, $ZrTiO_4$, La_2O_3, Ti and Zr solid phases.

Acknowledgments

This work was supported by the National Key R&D Program of China (2017YFB0306000, 2017YFB0305600), the Science and Technology Coordinating Innovative Engineering Project of the Shanxi province (2015KTZDGY09-04), the Postdoctoral Science Project of the Shanxi province (2017) and China Postdoctoral Science Foundation (2016M600770).

References

[1] S. Majumdar, I.G. Sharma, S. Raveendra, I. Samajdar, P. Bhargava, R. Tewari, A study on preparation of Mo–0.6Ti–0.2Zr–0.02C alloy by mechanical alloying and hot isostatic pressing, and its characterization, Mater. Chem. Phys. 113 (2009) 562–566.
[2] S. Majumdar, I.G. Sharma, S. Raveendra, I. Samajdar, P.R. Bhargava, In situ chemical vapour co-deposition of Al and Si to form diffusion coatings on TZM, Mater. Sci. Eng. A 492 (2008) 211–217.
[3] G. Filacchioni, E. Casagrande, U. De Angelis, G. De Santis, D. Ferrara, Effects of strain rate on tensile properties of TZM and Mo–5%Re, J. Nucl. Mater. 705 (2002) 307–311.
[4] T.S. Byun, M. Li, B.V. Cockeram, L.L. Snead, Deformation and fracture properties in neutron irradiated pure Mo and Mo alloys, J. Nucl. Mater. 376 (2008) 240–246.
[5] B.V. Cockeram, The mechanical properties and fracture mechanisms of wrought low carbon arc cast (LCAC), molybdenum–0.5pct titanium–0.1pct zirconium (TZM), and oxide dispersion strengthened (ODS) molybdenum flat products, Mater. Sci. Eng. A 418 (2006) 120–136.
[6] B.V. Cockeram, R.W. Smith, L.L. Snead, The influence of fast neutron irradiation and irradiation temperature on the tensile properties of wrought LCAC and TZM molybdenum, J. Nucl. Mater. 346 (2005) 145–164.
[7] F. Dietmar, Murg W. Wolfgang, W. Laufenberg, Molybdenum powder mixture for TZM, Jul. 25 (1995), Patent Number 5435829.
[8] S.B. Tan, L.Q. Liang, J. Liang, Y. Wang, R. Guo, High temperature performances

of Mo-La and TZM alloys, Rare Met. 30 (2006) 33–38.
[9] T. Mrotzek, A. Hoffmann, U. Martin, Hardening mechanisms and recrystallization behaviour of several molybdenum alloys, Int. J. Refract. Metals Hard Mater. 24 (2006) 298–305.
[10] L. Xu, S. Wei, D. Zhang, Y. Li, G. Zhang, J. Li, Fine structure and interface characteristic of α-Al_2O_3 in molybdenum alloy, Int. J. Refract. Metals Hard Mater. 41 (2013) 483–488.
[11] L.A. Diaz, A.F. Valdes, C. Diaz, A.M. Espino, R. Torrecillas, Alumina/molybdenum nanocomposites obtained in organic media, J. Eur. Ceram. Soc. 23 (2003) 2829–2834.
[12] L. Xu, S. Wei, J. Li, G. Zhang, B. Dai, Preparation, Preparation, microstructure and properties of molybdenum alloys reinforced by in-situ Al_2O_3 particles, Int. J. Refract. Metals Hard Mater. 30 (2012) 208–212.
[13] I.M. Gunter, J.H. Schneibel, J.J. Kruzic, Ductility and fracture toughness of molybdenum with $MgAl_2O_4$ additions, Mater. Sci. Eng. 458 (2007) 275–280.
[14] G. Liu, et al., Nanostructured high-strength molybdenum alloys with unprecedented tensile ductility, Nat. Mater. 12 (2013) 344–350.
[15] A.J. Mueller, R. Bianco, R.W. Buckman, Evaluation of oxide dispersion strengthened (ODS) molybdenum and molybdenum ± rhenium alloys, Int. J. Refract. Metals Hard Mater. 4–5 (1999) 205–211.
[16] H.C. He, K.S. Wang, P. Hu, X.Q. Kang, P. Wang, R.Z. Liu, Fracture and microstructure of La doped TZM plate, Rare Metal Mater. Eng. 04 (2014) 964–967.
[17] H.C. He, K.S. Wang, P. Hu, X.Q. Kang, P. Wang, R.Z. Liu, Effects of rare earth La element doping on recrystallization behavior of TZM alloy sheet, Rare Metal Mater. Eng. 05 (2015) 1297–1300.
[18] X.Q. Kang, K.S. Wang, Z. Zhang, P. Hu, H.C. He, Effect of lanthanum doping method on properties of La-TZM alloy, Rare Metal Mater. Eng. 05 (2015) 1254–1258.
[19] K.S. Wang, J.F. Tan, P. Hu, Z.T. Yu, F. Yang, B.L. Hu, La_2O_3 effects on TZM alloy recovery, recrystallization and mechanical properties, J. Mater. Sci. Eng. A 636 (2015) 415–420.
[20] F. Yang, K.S. Wang, P. Hu, H.C. He, X.Q. Kang, H. Wang, La doping effect on TZM alloy oxidation behavior, J. Alloys. Compd. 593 (2014) 196–201.
[21] P. Hu, K.S. Wang, F. Yang, H.C. He, X.Q. Kang, H. Wang, Z.T. Yu, J.F. Tan, Preparation and oxidation behavior of La-TZM alloy plates, J. Rare Metal Mater. Eng. 07 (2014) 1722–1726.
[22] P. Hu, K.S. Wang, F. Yang, H.C. He, X.Q. Kang, H. Wang, Z.T. Yu, J.F. Tan, Preparation and properties of La-TZM alloy by substitution of organic carbon for graphite, J. Rare Metal Mater. Eng. 06 (2014) 1502–1506.
[23] P. Hu, F. Yang, K.S. Wang, Z.T. Yu, J.F. Tan, R. Song, The influences of La doping method on the microstructure and mechanical properties of Mo alloys, Int. J. Refract. Metals Hard Mater. 52 (2015) 131–136.
[24] G. Liu, G.J. Zhang, F. Jiang, X.D. Ding, Y.J. Sun, J. Sun, E. Ma, Nanostructured high-strength molybdenum alloys with unprecedented tensile ductility, Nat. Mater. 3544 (2013) 344–350.
[25] J. Liang, Z.P. Xi, H.P. Tang, L.P. Li, Mechanism analysis of carbide formation in tzm alloy, J. Rare Metal Mater. Eng. (2011) 210–214.
[26] J.L. Fan, M.Y. Lu, H.C. Cheng, J.M. Tian, B.Y. Huang, Effect of alloying elements Ti, Zr on the property and microstructure of molybdenum, Int. J. Refract. Metals Hard Mater. 27 (2009) 78–82.
[27] P.N. Browning, J. Fignar, A. Kulkarni, Sintering behavior and mechanical properties of Mo-TZM alloyed with nanotitanium carbide, Int. J. Refract. Metals Hard Mater. 62 (2017) 78–84.
[28] S.K. Kar, V.S. Dheeradhada, D.M. Lipkin, Phase Stability in the Mo-Ti-Zr-C System via, thermodynamic modeling and diffusion multiple validation, Miner. Metall. Proc. 44 (2013) 3999–4010.
[29] W. Li, G. Zhang, S. Wang, B. Li, J. Sun, Ductility of Mo–12Si–8.5B alloys doped with lanthanum oxide by the liquid–liquid doping method, J. Alloys. Compd. 642 (2015) 34–39.
[30] P. Hu, K.S. Wang, H.C. He, X.Q. Kang, H. Wang, P.Z. Wang, Preparation and properties of La-TZM alloy plates, Appl. Mech. Mater. 320 (2013) 350–353.
[31] T. Mrotzek, A. Hoffmann, U. Martin, Hardening mechanisms and recrystallization behavior of several molybdenum alloys, Int. J. Refract. Metals Hard Mater. 24 (4) (2006) 298–305.
[32] G. Liu, G.J. Zhang, F. Jiang, Nanostructured high-strength molybdenum alloys with unprecedented tensile ductility, Nat. Mater. 12 (2013) 344–350.
[33] S.K. Kar, V.S. Dheeradhada, D.M. Lipkin, Phase stability in the Mo-Ti-Zr-C system via, thermodynamic modeling and diffusion multiple validation, Metall. Mater. Trans. 44 (2013) 3999–4010.
[34] J. Wadsworth, A reevaluation of the mechanical properties of molybdenum- and tungsten-based alloys containing hafnium and carbon, Metall. Trans. A 14 (1983) 285–294.